Nuclear Science and Techniques (2024) 35:149
https://doi.org/10.1007/s41365-024-01499-x

Simulation study of the performance of the Very Large Area gamma-ray Space Telescope

Xu Pan[1,2] · Wei Jiang[1] · Chuan Yue[1] · Shi-Jun Lei[1] · Yu-Xin Cui[1,2] · Qiang Yuan[1,2]

Received: 30 October 2023 / Revised: 27 February 2024 / Accepted: 10 March 2024 / Published online: 29 August 2024

Abstract
The Very Large Area gamma-ray Space Telescope (VLAST) is a mission concept proposed to detect gamma-ray photons through both Compton scattering and electron–positron pair production mechanisms, thus enabling the detection of photons with energies ranging from MeV to TeV. This project aims to conduct a comprehensive survey of the gamma-ray sky from a low-Earth orbit using an anti-coincidence detector, a tracker detector that also serves as a low-energy calorimeter, and a high-energy imaging calorimeter. We developed a Monte Carlo simulation application of the detector using the GEANT4 toolkit to evaluate the instrument performance, including the effective area, angular resolution, and energy resolution, and explored specific optimizations of the detector configuration. Our simulation-based analysis indicates that the current design of the VLAST is physically feasible, with an acceptance above 10 m^2 sr which is four times larger than that of the Fermi-LAT, an energy resolution better than 2% at 10 GeV, and an angular resolution better than 0.2° at 10 GeV. The VLAST project promises to make significant contributions to the field of gamma-ray astronomy and enhance our understanding of the cosmos.

Keywords Space astronomy · Gamma-ray telescope · Calorimeter Monte Carlo simulation

1 Introduction

Gamma-ray astrophysics is an exciting field in astronomical science that has received significant attention. Detecting cosmic gamma-ray emissions in the energy range from MeV to GeV is difficult using ground-based telescopes and is preferably performed in space. Gamma ray telescopes covering this energy range can be roughly divided into two categories based on the detection principle: pair-production telescopes and Compton-scattering telescopes. For pair-production telescopes, the OSO-3 [1] provided the first confirmation that the detection of gamma rays is feasible for complex backgrounds of charged particles. Breakthrough discoveries of high-energy gamma-ray observations were carried out using SAS-2 [2] and COS-B [3] missions in the 1970 s. In the 1990 s, EGRET made significant progress in surveying the gamma-ray sky above 50 MeV, leading to the discovery of numerous high-energy gamma-ray sources [4]. The Fermi LAT gamma-ray space telescope [5], launched in 2008, has been highly successful in this field for over a decade, identifying more than 6000 gamma-ray sources in its fourth catalog [6]. However, owing to the limited acceptance and angular resolution of detectors, nearly one-third of the sources remain unidentified. The GAMMA-400 space mission, installed on the Russian Navigator space platform, is currently under preparation. With its excellent energy resolution and unprecedented angular resolution above 30 GeV compared to other space-based systems, it has the potential

This work was supported by the National Key Research and Development Program of China (No. 2021YFA0718404), the National Natural Science Foundation of China (Nos. 12220101003, 12173098, U2031149), the Project for Young Scientists in Basic Research of Chinese Academy of Sciences (CAS) (No. YSBR-061), the Scientific Instrument Developing Project of CAS (No. GJJSTD20210009), the Youth Innovation Promotion Association of CAS, and the Young Elite Scientists Sponsorship Program by the China Association for Science and Technology (No. YESS20220197).

✉ Qiang Yuan
yuanq@pmo.ac.cn

[1] Key Laboratory of Dark Matter and Space Astronomy, Purple Mountain Observatory, Chinese Academy of Sciences, Nanjing 210023, China

[2] School of Astronomy and Space Science, University of Science and Technology of China, Hefei 230026, China

to unlock new insights in this field. However, its effective area is limited to 4000 cm^2, owing to the size of the detector [7]. The pioneering Compton-scattering telescope for opening the MeV gamma-ray astronomical window was COMPTEL [8]. Another small detector onboard the Chinese space station, POLAR [9], is dedicated to measuring the polarization of MeV gamma rays through Compton scattering. The COSI [10] project, which is funded by NASA's Small Explorer program, is scheduled for launch in 2026 and features an exceptional energy resolution. The effective area of COSI remains small and perhaps does not meet the requirements of a powerful detector for MeV time-domain astronomy. Recent advancements in detection technology (semiconductors, scintillators, and time-projection chambers) have sparked growing interest in the MeV energy band. Consequently, several space-based gamma-ray missions have been proposed in recent years, such as PANGU [11], AMEGO [12], e-ASTROGAM [13], AdEPT [14], and GECCO [15], MAST [16], GRAMS [17], XGIS-THESEUS [18], Crystal Eye [19], and MASS [20]. With ongoing developments in detection technology and increasing scientific demand, there is a pressing need for gamma-ray telescopes with enhanced sensitivity.

We propose the Very Large Area gamma-ray Space Telescope (VLAST) [21–24] with a significantly larger effective area, four times larger than Fermi-LAT. VLAST primarily consists of an Anti-Coincidence Detector (ACD), a Silicon Tracker, a low energy gamma-ray detector (STED), and a high-energy imaging calorimeter (HEIC), combining the advantages of DAMPE [25] and APT [26]. The STED design can measure both low-energy Compton scattering and high-energy pair production events, which change the traditional tungsten plate to a thin cesium iodide (CsI) tile, allowing model-independent control of the systematic detector uncertainties. VLAST can survey the gamma-ray sky from a low Earth orbit in the energy band from approximately 0.1 MeV to more than 1 TeV.

The key scientific goals of the VLAST include (i) searching for dark matter signatures in galaxy cores, galaxy disks, and dwarf galaxies [27–31], (ii) monitoring special gamma-ray sources over time, such as Active Galactic Nuclei, gamma-ray bursts, millisecond pulsars, and supernovas [32–37], (iii) understanding the origin and transportation of cosmic rays [38–40], (iv) using extragalactic diffuse gamma-rays and gamma-ray horizons to study the evolution of the universe [41–44], (v) testing fundamental physical laws, such as the Lorentz invariance and equivalence principle [45–48], and so on.

In this study, we evaluated the performance and optimized the design of VLAST using simulations. The simulation framework was developed based on the GEANT4 [49]. For event reconstruction, different energy or trajectory reconstruction algorithms were used to analyze the Compton scattering and pair production events. The key performance parameters of VLAST were obtained based on detailed MC simulations, such as acceptance, effective area, angular resolution, energy resolution, and e-p discrimination. Furthermore, some specific design parameters were optimized, such as the threshold of ACD, the size of ACD, the width of the silicon strip pitch, and the number of CsI layers in the STED.

2 Baseline design of VLAST

VLAST follows the foundational principles and structures of earlier gamma detectors. The detector included three primary subdetectors: ACD, STED, and HEIC. The ACD plays a critical role in rejecting the charged particle background and reducing backsplashes from high-energy events. STED, which shares design similarities with APT, replaces the tungsten plate in the tracker detector with thin CsI tiles. This alteration allows for the measurement of Compton events and pair production events, thus enabling the tracking of their trajectories to reconstruct the direction of the incident gamma rays. Low-energy MeV photons are primarily measured through Compton scattering with electrons to determine their energy and direction of incidence. The HEIC measures the energy of incident particles and images the profile of the electromagnetic or hadron shower of high-energy particles, which is used to discriminate between electrons and protons and provides an estimated direction of the incident particle. Figure 1 presents a schematic of the VLAST detector.

2.1 Anti-coincidence detector

The primary function of the ACD is to minimize the backsplash effect caused by high-energy photons and to reject the background of the charged particles. As the first barrier for rejecting charged particles, it is closely wrapped around the STED. The ACD is composed of 448 plastic scintillator detector tiles (20 cm ×20 cm ×1 cm). Plastic scintillators have a high detection efficiency for charged particles and a low detection efficiency for photons. Therefore, they are often used as the ACD for gamma-ray detection. To prevent particles from passing through the gap between the ACD without being identified, the gaps between the tiles are covered by flexible scintillating fiber ribbons.

The backsplash effect was first discovered by the EGRET team. When a high-energy photon enters the calorimeter, it generates numerous secondary low-energy photons (ranging from 0.1 MeV to a few MeV), some of which may travel in the opposing direction through the STED and reach the ACD. This scattering causes the electrons to recoil, thus generating an electrical signal in the ACD. The intensity of this effect depends on many factors, such as the incident particle energy, calorimeter thickness, and material

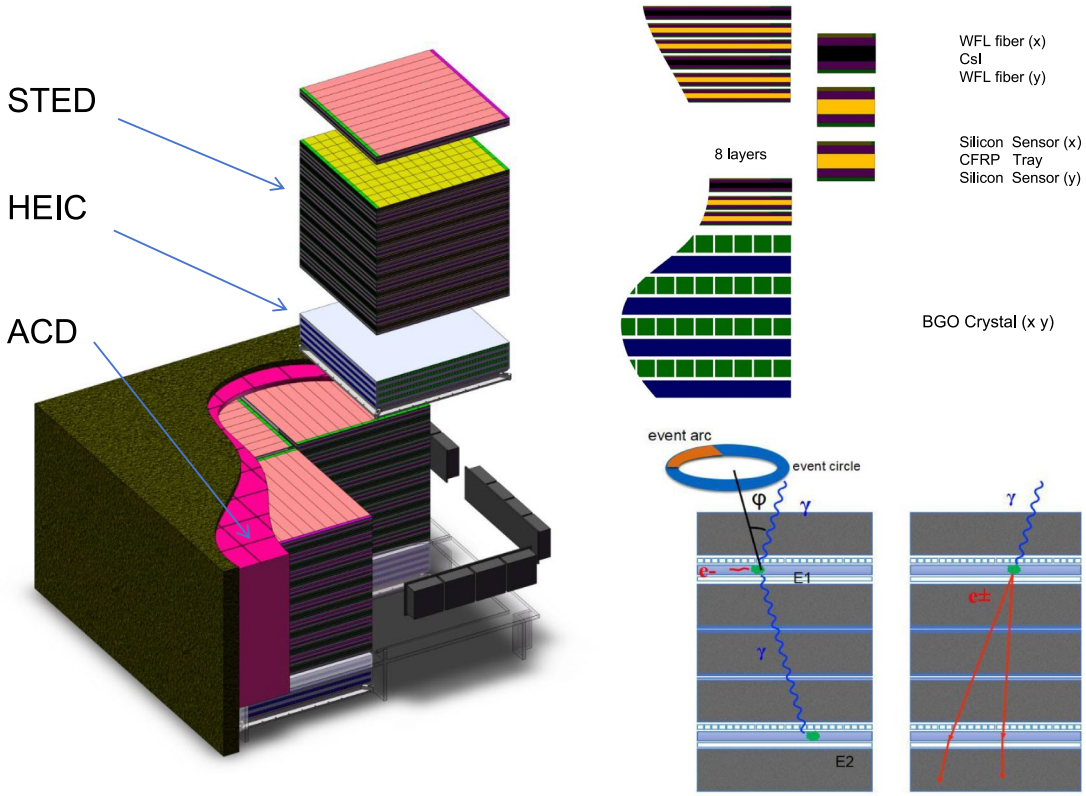

Fig. 1 (Color online) Schematic of the VLAST detector. The ACD covers the whole detector except the bottom. The STED has a total of 8 layers, each containing one sub-layer of CsI crystals connected to wavelength-shifting fibers and two sub-layers of silicon strip modules. The HEIC is placed below the STED, which contains four layers of orthogonally arranged Bismuth Germanium Oxide (BGO) crystals. The bottom right panel shows the two classes of events detectable by VLAST, the Compton scattering events and the electron–positron pair production events

composition. The intensity of the backsplash effect increases with the energy of the incident particles and the radiation length of the calorimeter. To mitigate this effect, the Fermi-LAT detector divides the ACD into smaller units by utilizing the discrepancy between the piece in the incident direction and that in the recoil to discriminate the recoil event. This modular design effectively suppresses the misinterpretation of photons attributed to the backsplash effect of high-energy photons. Following this scheme, the ACD in the VLAST design enables the dismissal of fired tiles that are not aligned with the direction of photon incidence, thereby significantly mitigating the influence of the backsplash effect. The backsplash effect in VLAST is shown in Fig. 4.

The photon flux is lower than that of protons by a factor of 10^5 and lower than that of electrons by approximately 10^3 in the observational energy band of VLAST. To detect photons in the complex cosmic-ray background of charged particles, VLAST must have an outstanding ability to distinguish between photons and charged particles. When photons transform into electron–positron pairs in the STED, they can be discriminated from protons based on the shower pattern produced by the electrons-positrons and protons in the HEIC. As described in Sect. 4.5, HEIC has good electron-to-proton (e-p) discrimination capability, which significantly reduces the proton background. However, the discrimination between photons and electrons depends only on the ACD, which requires a minimum rejection fraction of 0.999 for charged particles. Therefore, ACD plays a critical role in identifying photons and distinguishing them from charged particles in the VLAST detector.

2.2 Silicon tracker and low energy gamma-ray detector

The STED of VLAST is designed to fulfill three primary functions. First, it reconstructs particle trajectories with an accuracy exceeding 120 μm for most incident particles. Second, it determines the charge of cosmic rays. Lastly, it converts the incoming photons into electron–positron pairs and detects both the photons and electrons resulting from Compton scattering. It consists of eight layers of silicon trackers and low-energy gamma-ray detector modules. Each module consists of a CsI layer on the top and a silicon strip module at the bottom. The silicon strip module contains two layers

of silicon strip detectors. The single-sided silicon strips are arranged in the x- and y-directions with a pitch size of 120 μm, defined as the distance between the centers of the adjacent strips. The top six layers of the 8-layer CsI have a thickness of 2 mm each, and the bottom two layers have a thickness of 4 mm each, resulting in a total radiation length of approximately 1 X_0. Each layer of CsI is assembled by joining numerous CsI (Na) scintillating crystal square panels, with each panel side measuring approximately 200 mm. The upper and lower surfaces of each layer of CsI are tightly coupled to two layers of square wavelength-shifting (WLS) fibers arranged along the x- and y-axes, each with a cross-sectional side length of 2 mm. The WLS fibers absorb the blue scintillation light emitted from the CsI and transmit a fraction of the re-emitted red light to the SiPMs connected at their ends. The readout signals from the SiPMs can be used to infer the energy deposition and $x-y$ coordinates of particle interactions in the CsI panels.

There are two main types of interactions between gamma rays in the STED: Compton scattering and pair production. The dominant interaction depends on the energy of the gamma rays. Compton scattering is predominant at energies below a few tens of MeV, whereas electron–positron pair production dominates at higher energies. Different types of detectors have been designed to capture gamma rays in various energy bands. For example, COMPTEL [8], Fermi-LAT [5], and AGILE [50] focused on either the low- or the high-energy range. In contrast, VLAST aims to simultaneously detect gamma rays in the energy band simultaneously from 0.1 MeV to 1 TeV, encompassing both interactions. Consequently, the gamma rays undergoing these two distinct interactions require different detection methods. The detection principle of VLAST is illustrated in the lower-right panel of Fig. 1.

For pair production events, the conceptual design of VLAST is similar to that of Fermi-LAT and AGILE, but is optimized for the lower energy band. CsI serves a dual role as both a positron-electron pair converter and detector for measuring the position and low-energy deposition of interactions.

This design ensures a high conversion efficiency of gamma rays into electron–positron pairs. The CsI low-energy calorimeter does not reduce the multiple scattering effects of pair events. However, it can provide the deposited energy and position of the fired tiles better than tungsten plates, allowing for a more accurate assessment of energy and multiple scattering. Consequently, this design improves the energy and angular resolution at low energies compared to Fermi-LAT and AGILE.

Detection of a Compton scattering event is challenging because the scattered photons carry away a significant portion of the momentum of the primary particle, especially when compared to pair production processes. Therefore, VLAST must be capable of simultaneously measuring two photons. Upon the entry of an incident photon into the detector, Compton scattering occurs within one layer of the tracker, giving rise to secondary photons and electrons. The photon is scattered with an electron in the detector and transfers a fraction of its energy (E_1) to an electron. The scattered photon retains its remaining energy (E_2) and may interact with the CsI of the lower-energy detector behind it or enter the HEIC. The angle θ between the photon and the electron after Compton scattering is calculated as follows:

$$\cos(\theta) = 1 - m_e c^2 \left(\frac{1}{E_2} - \frac{1}{E_1 + E_2} \right), \tag{1}$$

where $m_e c^2$ is the mass-equivalent energy of electron.

If only the angle of Compton scattering can be reconstructed, the incident direction of the photon can only be located on a circle in the sky, which is referred to as an “event circle". These events are known as “untracked" events. The width of the circle is related to the accuracy of the detector in measuring the direction of the scattered photon and energy of the scattered electron. If the direction of the scattered electrons can be measured, the “event circle" becomes an “event arc". These events are referred to as “tracked" events, and the length of the arc reflects the accuracy of the directional measurement of the scattered electron. However, measuring such events is difficult for VLAST because the scattered electrons are easily absorbed by the CsI low-energy detector.

The STED has a total thickness equivalent to one radiation length, which allows for a 65% conversion rate of high-energy photons at normal incidence into electron–positron pairs. Figure 2 illustrates the conversion positions. Figure 3 provides an orthogonal cut view of a 50 MeV gamma-ray event detected in the tracker, demonstrating the generation of an electron–positron pair in the CsI crystal and the gradual deviation of the electron and positron from their original paths owing to multiple scattering. Recoil particles cause signal scattering. This inverted “V” signature is helpful in rejecting the much larger background of charged cosmic rays.

The main design challenge of STED is to balance the electron–positron pair conversion efficiency with the angular resolution in the low-energy range. The angular resolution of the low-energy photons is significantly affected by multiple scattering, which depends on $1/E$. Therefore, it is necessary to design thinner CsI conversion materials to reduce multiple scattering effects. However, this approach reduces the conversion efficiency of low-energy photons. To resolve this tradeoff, CsI is divided into two types: thin layers are placed in the front section of the STED to ensure angular resolution for low-energy photons, and thick layers are placed in the back to maintain a high conversion

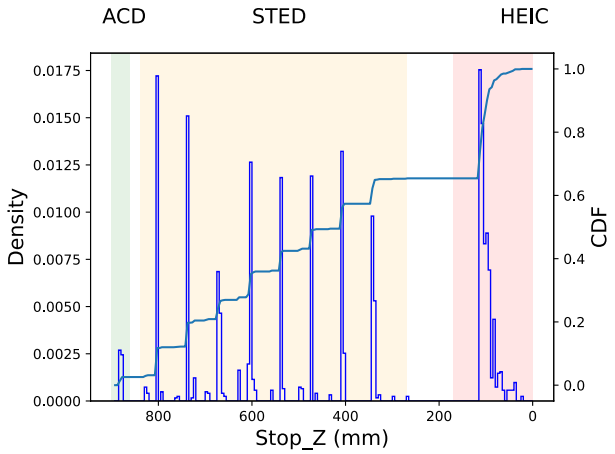

Fig. 2 (Color online) The position distribution of 50 GeV photons converting into positron-electron pairs. From left to right, the peaks correspond to the ACD, STED, and HEIC, respectively. The cumulative distribution function (CDF) of conversion probabilities is displayed by the *y*-axis on the right side of the figure

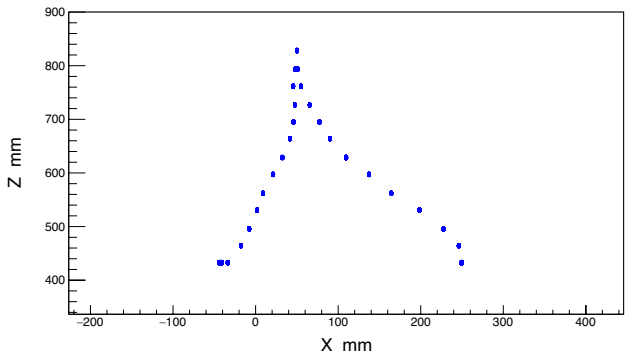

Fig. 3 Illustration of the hits in the STED for a 50 MeV gamma-ray photon ($x-z$ plane). The photon converts into an electron–positron pair in one of the CsI plates

efficiency for high-energy photons. For low-energy photons with energies of approximately 100 MeV, the direction is mainly determined by the two leading measurement points. The first two measurement points after the photon transition point are crucial in accurately reconstructing the direction of incident photons. To reduce the multiple scattering effects caused by the CsI plate and support material, the efficiency of each measurement layer should be close to 100%. Therefore, the spaced placement of CsI planes with silicon strip planes allows the precise measurement of positive and negative electron traces. The thick CsI plane placed at the bottom increases the efficiency of photon conversion at lower energies. This increases the statistics of low-energy photons. Studying the time-domain variation of photons is essential, despite the reduced angular resolution of photons.

Another challenge is balancing the field of view (FoV) and angular resolution of the detector. For very-high-energy photons, the impact of multiple scattering on the angular resolution becomes less critical. The ratio between the width of the silicon strip and the thickness of the silicon tracker detector places the primarily limitation on the angular resolution. Ideally, finer silicon strips would yield improved angular resolution. However, this results in an increased complexity of the fabrication process and higher electronic power consumption. By contrast, increasing the thickness of the STED leads to a reduction in the FoV and shifts the center point of the detector upward. STED was designed with these factors in mind.

2.3 High energy imaging calorimeter

The HEIC has two main purposes. First, it measures the deposited energy of particles resulting from the interaction of incident photons. Second, it images the shower development profile which is used to reject the cosmic ray background and to estimate the energy leakage fluctuations in the shower. To achieve high energy resolution, we adopted the design of the BGO calorimeter onboard the DAMPE [25]. The HEIC comprises four identical modular towers arranged in a 2×2 array; each tower has 416 BGO crystals divided into four layers, with each adjacent layer placed orthogonally. Each BGO crystal is 2.5 cm × 2.5 cm × 1.4 m in size. The total vertical depth of HEIC is 18 radiation lengths or 1 nuclear action length, with oblique incidence events experiencing higher radiation lengths. The total effective detection area of HEIC is at last 2.8 m × 2.8 m. Photomultipliers at both ends read out the signals from the BGO bars. The different dynodes of the photomultiplier tubes are responsible for different energy bands, enabling VLAST to encompass a wide energy range from MeV to TeV. The left/right light asymmetry provides a measure of the position of the energy deposit along the bar. Thus, each fired BGO crystal provides the x, y, and z coordinates of the shower, and the shower shape can be inscribed in three dimensions. The number of inscribed pixels is directly related to the crystal dimensions. The shower axis also provides a rough track that can be used as a seed for the STED track reconstruction. Energy leakage is inevitable for grazing incidence and very high-energy photons, because the calorimeter has a limited radiation length. Leakage energy can be estimated using a shower profile from beam tests or simulations. Taking the energy leakage correction into account significantly enhances the energy resolution of these events.

3 Simulation and event reconstruction

3.1 Simulation

To validate and optimize the VLAST design concepts, we developed a simulation framework that includes incident particle definition, detector geometry definition, a physical interaction list, digitization, and an event reconstruction analysis system. The framework is based on GEANT4, a publicly available toolkit developed in C++ used to simulate the interactions between particles and matter. It includes numerous physical models of particle–matter interactions and is widely used in various fields, such as high-energy physics, accelerator physics, space science, and medicine [49, 51–54]. The gamma-ray source is set up as a sphere with an energy range of 0.1 MeV–1 TeV.

The GEANT4 FTFP_BERT physics list was used to simulate incident particles with energies above 10 MeV. For 0.1 MeV–10 MeV gamma rays, we substituted electromagnetic physics with G4EmStandardPhysics_option4. This option introduces a more accurate model of Compton scattering and low-energy electromagnetic interactions, albeit at the cost of significantly increasing the computation time. We used the geometry module of GEANT4 to build the entire detector system, including the ACD, STED, and HEIC. The constructed VLAST geometry with a normal-incident 50 GeV gamma ray is shown in Fig. 4. The simulated output data of different subdetectors were digitized with the typical electronic noise of their corresponding readout systems [55].

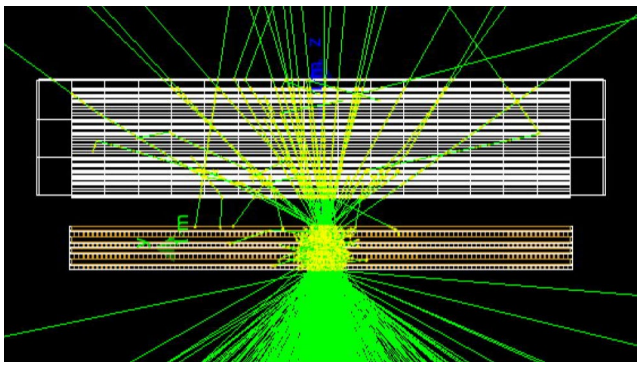

Fig. 4 (Color online) Simulated shower particle tracks for a normal-incident 50 GeV photon. The backsplash particles would produce self-veto in the ACD

3.2 Trigger design

The preliminary trigger logic for scientific data collection consists of five trigger engines: MeV-Gamma, GeV-Gamma, low-energy (LE), high-energy (HE), and Calibration, as shown in Table 1. Each subdetector provides one or more trigger requests as detailed in the following list:

- ACD: energy > 0.8 MeV, corresponding to 0.4 MIP (minimum ionization particle);
- STED: three consecutive layers are on fire;
- CsI-hit: two layers are on fire;
- HEIC-hit: > 5 MeV for the first or second layer;
- HEIC-HE: > 5 MeV,> 500 MeV,> 500 MeV,> 500 MeV for the first 4 layers;
- HEIC-LE: > 5 MeV, > 5 MeV, > 50 MeV, > 50 MeV for the first 4 layers;
- HEIC-MIP: > 5 MeV for the 1st, 2nd, 7th, and 8th layers.

The MeV-Gamma, GeV-Gamma, and HE trigger logics were combined to reserve gamma-ray events from sub-MeV to multi-TeV. The comprehensive trigger efficiencies were 45%, 90%, and >95% at 1 MeV, 1 GeV and above 10 GeV, respectively. LE trigger logic (with a large prescale factor) was designed to reserve GeV cosmic rays for performance validation in orbit. Calibration trigger logic was used for unit calibration of HEIC.

3.3 Event reconstruction

We utilized different algorithms to reconstruct the trajectories and energies of the pair production and Compton scattering events. The Kalman filter was used to reconstruct the trajectory of the pair production event after charge sharing. The Compton scattering formula was adopted to reconstruct the direction of photon incidence. The longitudinal development of an electromagnetic shower was used to reconstruct the energy.

Before trajectory reconstruction, the process of charge sharing between the silicon strips should be considered. This is

Table 1 Trigger logics of VLAST, including MeV-Gamma, GeV-Gamma, LE, HE and Calibration, and their corresponding requests (1: required; 0: excluded; ×: either)

	CsI-hit	HEIC-hit	HEIC-HE	HEIC-LE	HEIC-MIP	STED	ACD
MeV-Gamma	1	0	×	×	×	×	0
GeV-Gamma	×	1	0	×	×	1	0
LE	×	1	0	1	×	1	1
HE	×	1	1	×	×	×	×
Calibration	×	1	0	×	1	1	1

mainly due to diffusion during charge collection and capacitive coupling. The drifting of electron–hole pairs along the magnetic field lines causes the size of the charge cloud to increase, whereas capacitive coupling occurs on the coupling strip between the two readout strips. The charge-sharing parameters originating from DAMPE were obtained using a beam test [25, 56–60]. The charge-sharing algorithm is as follows:

$$E_k = E_i + 0.023 \cdot (E_{i-2} + E_{i+2}) + 0.0021 \cdot (E_{i-4} + E_{i+4}), \tag{2}$$

if the strip is a readout strip and

$$\begin{aligned} E_k =& E_i + 0.305 \cdot (E_{i-1} + E_{i+1}) + 0.062 \cdot (E_{i-3} + E_{i+3}) \\ &+ 0.012 \cdot (E_{i-5} + E_{i+5}) + 0.0024 \cdot (E_{i-7} + E_{i+7}). \end{aligned} \tag{3}$$

if the strip is a float strip. After the process of charge sharing, we combined the signals from neighboring silicon strips with a signal/noise ratio larger than four (19 keV) into a cluster, and then took the energy-weighted center as the position of the cluster. These clusters were used in the subsequent trajectory reconstruction analysis.

In this study, the Kalman filtering algorithm was employed to reconstruct the trajectory of the pair production event, a technique widely used in particle physics experiments [61–63]. When a gamma ray is converted into a pair in the CsI plane, the direction of the resulting electron/positron will experience a shift owing to multiple scattering effects during propagation. Hence, understanding the impact of multiple scatterings on the trajectory-reconstruction process is crucial. The Kalman filtering algorithm assesses and compensates for multiple scattering and measurement errors. This algorithm consists of three primary processes: prediction, filtering, and smoothing. The track direction in the kth layer was used to predict the hit position on the $(k+1)$th layer. Subsequently, the predicted hit position of the $(k+1)$th layer was adjusted using the measured hit. The evolution of the state vector is given by:

$$X_k = F_{k-1} X_{k-1} + W_{k-1}, \tag{4}$$

where X_k is the state vector that incorporates the position and momentum information in the kth layer, F_{k-1} is the propagation of the trail from the $(k-1)$th layer to the kth layer of the trail detector, and W_{k-1} is the random noise of the system. In dense media, tracking particles are subjected to random noise from multiple scattering, energy loss, and other physical processes that alter their trajectories. The trajectory offset caused by multiple scattering can be expressed as:

$$\sigma = \frac{13.6}{\beta c p} \sqrt{L/L_r} [1 + 0.038 \ln(L/L_r)], \tag{5}$$

where L is the thickness of CsI tile, L_r is the radiation length of CsI material, βc and p are the velocity and momentum (MeV) of the electron–positron pair, respectively. The measurement state vector is given by:

$$m_k = H_k X_k + V_k, \tag{6}$$

where m_k is the quantity measured by the kth layer, H_k is the measurement matrix, and V_k is the measurement error. Once a track had undergone a filtering process, it was smoothed. The trajectory parameters were further refined from bottom to top, in contrast to the filtering process. For further details, please refer to. [62, 64, 65].

The primary process for reconstructing the trajectory of MeV gamma rays involves identifying Compton scattering events and determining the sequence of scattering points. The CsI hit found from top to bottom with an energy deposition greater than 100 keV and no readout signals (less than 19 keV) from the silicon strips in the adjacent upper layer was considered the Compton scattering point.

Using the same method, additional isolated scattering points can be identified, and their scattering sequence and the probability of photoelectric effects can be analyzed based on the magnitude of energy deposition. We traced the photon trajectory after Compton scattering by connecting the first and second interaction points with the highest probability. According to the Compton scattering formula (1), reconstructions of the angle of Compton scattering do not determine the specific direction of the primary photon, but only fixes a ring in the sky. Multiple rings from the same source can be overlaid to locate the source.

For the electromagnetic shower induced by a high-energy photon, the overall deposited energy in CsI and BGO occupies most of the primary energy, despite a small fraction of energy loss. However, with an increase in incident energy, the longitudinal energy leakage becomes negligible, making the energy correction necessary to estimate the primary energy. The longitudinal segmentation of CsI and BGO allows a fit of the longitudinal shower profile, which provides a good way to correct the longitudinal energy leakage [66]. The longitudinal shower profile can be described using a gamma distribution formula, expressed as:

$$\frac{\mathrm{d}E(t)}{\mathrm{d}t} = E_0 \cdot \frac{(\beta t)^{\alpha-1} \cdot \beta \cdot e^{-\beta t}}{\Gamma(\alpha)}, \tag{7}$$

where $t = x/X_0$ represents the radiation length, $\Gamma(\alpha)$ is the gamma function, α and β are shape and scale factors, respectively. The depth of the shower maximum depends on α and β as $t_{\max} = (\alpha - 1)/\beta$. The value of $t_{\max}$ is closely correlated with the energy leakage ratio, offering an effective approach for energy correction [66].

4 Expected performance of the VLAST

4.1 Effective area

The effective area reflects the detection efficiency of the instrument. It is equivalent to the area of an ideal absorber that detects the same number of events as the real detector, considering event selection and reconstruction, within the same time. The effective area is calculated as [67]

$$A_{\mathrm{eff}}(E,\theta,\phi) = A_{\mathrm{geo}}(\theta,\phi)\varepsilon_{\mathrm{det}}(E,\theta,\phi)\varepsilon_{\mathrm{sel}}(E,\theta,\phi), \tag{8}$$

where $A_{\mathrm{geo}}(\theta,\phi)$ represents the geometric cross-sectional area of the instrument in a specific direction characterized by angles θ and ϕ, $\varepsilon_{\mathrm{det}}(E,\theta,\phi)$ is the detection efficiency, and $\varepsilon_{\mathrm{sel}}(E,\theta,\phi)$ is the selection efficiency. The detailed selection conditions for pair events include the following: (1) the trigger condition for particular event types is satisfied (MeV-Gamma, GeV-Gamma, or HEIC-HE); (2) the trajectory in the STED can be reconstructed correctly; and (3) the deposited energy in the ACD block in the direction of the reconstructed trajectory is below 0.5 MeV. The selection conditions for Compton events include the following: (1) no ACD readout exceeding 100 keV; (2) there are at least two CsI hits where the energy deposition at both points is greater than 100 keV and there is no readout signal (less than 19 keV) in the adjacent upper and lower layers of the silicon tracker detector; and (3) the energy deposition in the bottom CsI layer is less than 50 keV (to ensure that the majority of photon energy is deposited in the STED).

The effective area of VLAST is shown in Fig. 5. For Compton scattering events, the effective area is several thousand cm^2, surpassing the effective area of the COMPTEL detectors (10–50 cm^2) by one or two orders of magnitude. It also has a larger effective area than planned MeV detectors such as the e-ASTROGAM, AMEGO, GECCO, and XGIS-THESEUS detectors. Furthermore, the effective area for pair production events exceeds 4 m^2 above 1 GeV under normal incidence, which is four times larger than that of the Fermi-LAT detector. However, the effective area slightly decreases for 30° and 45° incidence angles for both Compton scattering and pair production events. Figure 6 shows the effective area as a function of the particle incidence angle at different energies (50 GeV and 100 GeV). The effective area diminishes gradually with an increase in the angle of incidence, and the maximum off-axis incidence angle can reach 70°. The FoV of VLAST is 2.5 sr.

The acceptance of a gamma-ray detector refers to the portion of incoming gamma rays that the detector is capable of capturing or detecting. A larger acceptance indicates that the detector can detect gamma rays from a wider portion of the sky, thereby increasing its sensitivity for gamma-ray detection. The primary design concept of

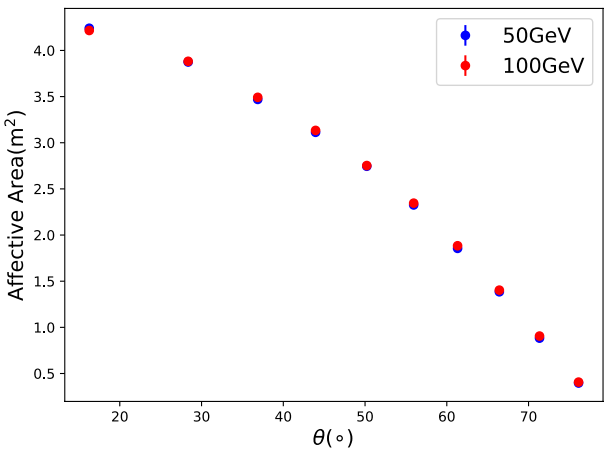

Fig. 6 Effective area for gamma rays with different incident angles

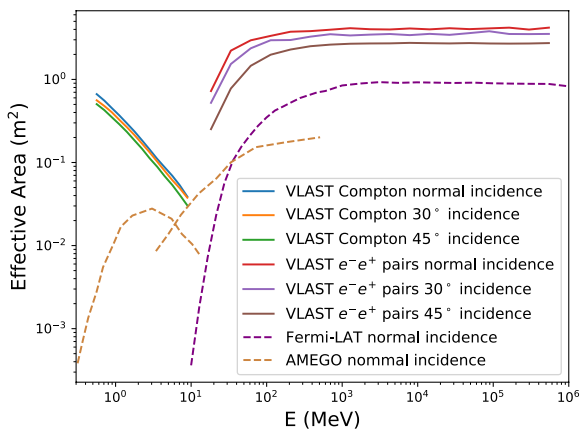

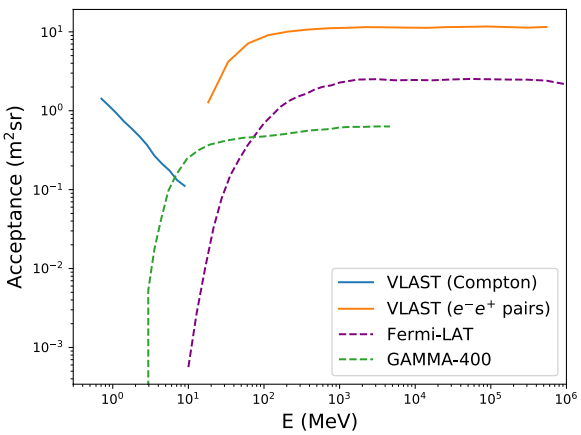

Fig. 5 (Color online) Left: effective areas of VLAST for photon events with normal incidence, 30°, and 45° incident angles, compared with those of AMEGO [12, 68] and Fermi-LAT [69]. Right: acceptance of the VLAST for gamma rays of different energies, compared with results of GAMMA-400 [7] and Fermi-LAT [69]

VLAST is to substantially enhance the acceptance of the detector to capture more photons and achieve more precise measurements with increased statistical significance. Therefore, the acceptance of VLAST must be sufficiently high. Acceptance is defined as the integral of the effective area over the solid angle $G(E) = \int_{\Omega} A_{\rm eff}(E, \theta, \phi) {\rm d}\Omega$. The acceptance of VLAST is shown in Fig. 5. For Compton scattering events, the maximum value of acceptance is several m^2 sr. As the energy increases from MeV to GeV, the acceptance gradually rises from 1.6 to 12 m^2 sr. In the design of VLAST, CsI crystal plates replace the tungsten foils used in many other gamma-ray detectors to enhance pair conversion. This substitution significantly improves the acceptance in the MeV energy range compared to Fermi-LAT. Given its substantial size, the acceptance of VLAST reaches 12 m^2 sr in the energy range above GeV.

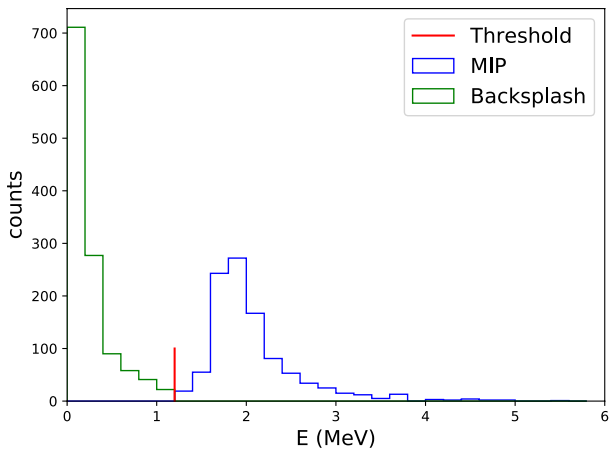

Fig. 7 Energy deposition distribution of MIPs and backsplash effect in the ACD. The optimized threshold that balances the high detection efficiency of charged primary particles and low contamination of backsplash is marked out in the plot

4.2 Self-veto

The detailed settings of the ACD need to be optimized, including the detection threshold and the size of the ACD. The detection threshold of the ACD must strike a balance between the detection efficiency of charged particles and suppression of backsplash effects. To improve the efficiency of detecting charged particles that exhibit a Landau distribution in the energy deposition within the ACD, the detection threshold should be lowered. However, to reduce the weak signals from recoil particles, the detection threshold should be set higher. The conflict between these two requirements is illustrated in Fig. 7. We used the false veto ratio of gamma rays to determine the threshold. Gamma ray photons may be misidentified as charged particles and subsequently rejected because of the backsplash effect. Even if photons do not leave a signal when passing through the ACD, low-energy recoil photons can trigger the ACD. Consequently, the tile in the direction of the particle could exhibit a signal, leading to the event being incorrectly identified as a charged particle. The false veto ratio is defined as $f = N_{\rm wrong}/N_{\rm total}$, where $N_{\rm wrong}$ are the photons misidentified as charged particles and $N_{\rm total}$ is the total number of incident photons. The false veto ratio as a function of the energy is shown in the left panel of Fig. 8. The higher the photon energy, the greater the probability that it will be misclassified as a charged particle. The middle panel of Fig. 8 presents the gamma-ray false veto ratios at different detection thresholds. For an ACD of size 20 cm × 20 cm, we determined that the optimized threshold value was 0.5 MeV where the gamma false veto rate was less than 15%. The size of the ACD should also be set reasonably. Under ideal conditions, a smaller ACD block results in a better suppression of the backsplash effect. However, this also requires more readouts and higher power consumption. Thus, to achieve the desired performance under limited conditions, tests were conducted to evaluate the suppression of the backsplash effect for different ACD sizes. The results of these tests are shown in the right panels of Fig. 8. An ACD tile size of 20 cm × 20 cm is reasonable when the false gamma veto rate is below 15%. Optimization

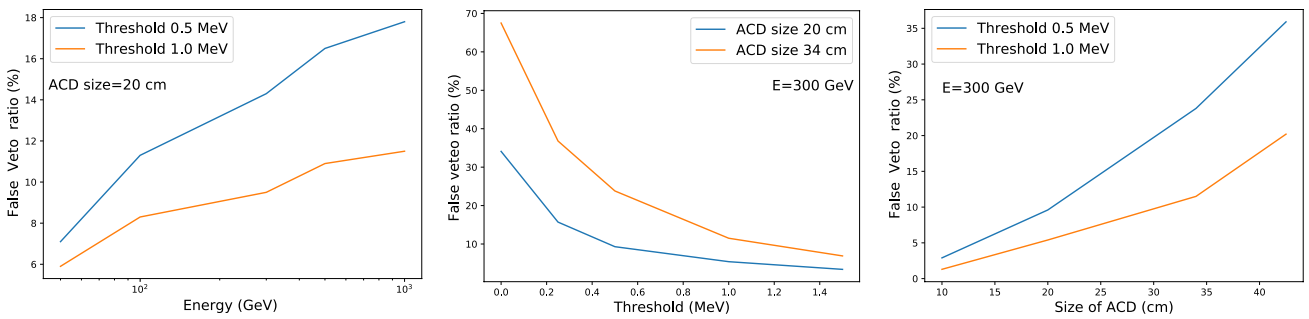

Fig. 8 (Color online) False veto ratios as functions of incident energy (left), the ACD threshold (middle), and the ACD size (right)

of the ACD thickness is also necessary. The ACD must be sufficiently thick to generate adequate fluorescence, ensuring the effective detection of charged particles. However, it should not be excessively thick because this could lead to a significant number of photons interacting within the ACD being misidentified as charged particles. In this context, we set the thickness of the ACD to 1 cm, which is the same as that used for the Fermi-LAT. At this thickness, no more than 3% of the photons interact within the ACD. The interactions between photons within the ACD are illustrated in Fig. 2. Moreover, it is advisable to maintain wrapping materials around the ACD, such as micrometeoroid shields and thin thermal blankets. This precaution is important because charged cosmic rays can generate secondary photons that contribute to the local photon background upon interaction with such materials. This background can interfere with the accurate detection of gamma rays, thereby reducing the detection efficiency.

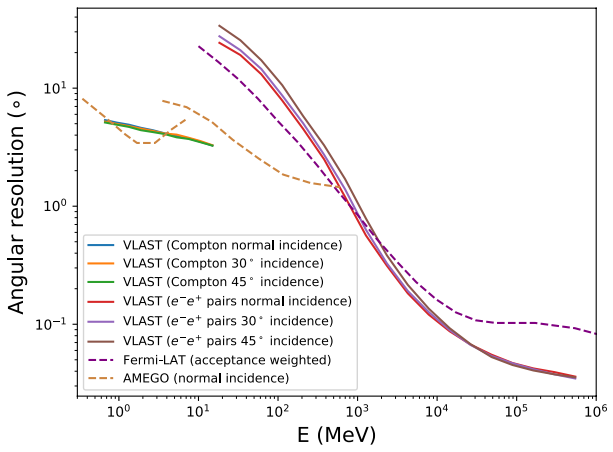

Fig. 9 (Color online) Angular resolution (68% containment) of VLAST for photon events with normal incidence, 30° and 45° off-axis angles, compared with results of AMEGO [12, 68] and Fermi-LAT [69]

4.3 Angular resolution

Angular resolution is another critical parameter of VLAST. A better angular resolution not only provides more accurate source positioning, but also results in a sharper profile of the point source. This, in turn, leads to a smaller contribution from the background, thereby increasing the sensitivity for detecting fainter sources. The angular resolution is defined differently for different interaction processes, namely Compton scattering and pair production processes. For Compton events, the angular resolution is defined as the sigma value obtained from the Gaussian fit to the distribution of the minimum angular distance between the nominal source position and the reconstructed event circle. For pair production events it is defined as the radius of the circle that includes 68% of the point-spread function (PSF). The PSF is determined using the angular distance between the source and the reconstructed direction.

The angular resolution of VLAST is shown in Fig. 9. To obtain these results, the same selection conditions as those described in Sect. 4.1 for calculating the effective area are used. For Compton events, the angular resolution is within the range of 4°–8°, which is comparable to AMEGO. Here, we present only the angular resolution of the untracked events. For pair production events, the angular resolution improves with increasing photon energy owing to the reduced impact of multiple scattering effects at higher energies. Notably, at 10 GeV, the angular resolution reaches 0.2 degrees. However, in the energy range of 10–10^3 MeV, the angular resolution is slightly worse than that of Fermi-LAT. In contrast, in the energy range above GeV, the angular resolution surpasses that of Fermi-LAT. This improvement can be attributed to our use of analog readout, whereas the Fermi-LAT employs a digital readout with silicon strips of approximately the same width.

As mentioned in Sect. 3.3, we implemented a spaced readout scheme for the silicon strip readout to reduce power consumption. However, VLAST requires a large number of electronic readouts, which results in substantial power consumption. To address this issue, we explored the use of digital readout, which records only the hit strips that exceed a signal threshold of 3σ above the baseline noise as "1," while unhit strips are recorded as "0." This implementation simplifies the electronics significantly and reduces the power consumption. We defined a cluster as the region of the hit silicon strips. For the digital readout, during cluster position reconstruction, the cluster position was set to the geometric center, whereas for analog readout, the energy-weighted average position was used for cluster reconstruction. Subsequently, track reconstruction was performed using Kalman filtering. A comparison of analog and digital readouts is shown in the left panel of Fig. 10. In the lower-energy range, the dominant error arises from multiple scattering, resulting in comparable angular resolutions for both analog and digital readouts. However, in the higher-energy range, measurement errors take precedence, and the geometric center of the cluster exhibits a significantly larger error than the energy-weighted center. This difference increases with energy, indicating that analog readouts provide better angular resolution than digital readouts.

We investigated the effect of different silicon strip widths on the PSF of VLAST for pair production events. Thinner strips offer a higher position measurement accuracy and better angular resolution. However, they require more electronic readouts, resulting in higher power consumption. Therefore, a balance between the angular resolution and

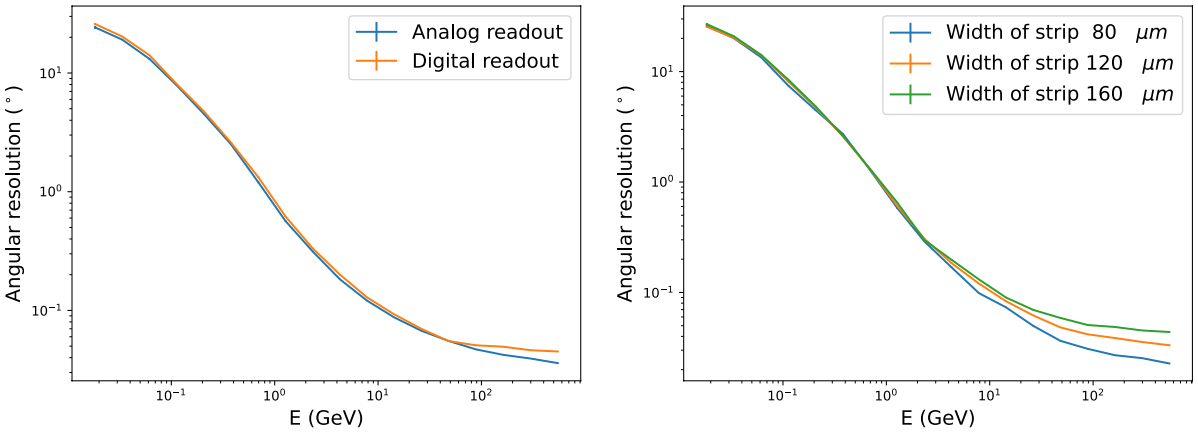

Fig. 10 (Color online) Angular resolution of VLAST for normal incident photons. The left panel shows the comparison between digital and analog readouts for a 120 μm strip width, and the right panel compares different widths of silicon strips for analog readout

power consumption is required. The tests were conducted using three widths: 80 μm, 120 μm, and 160 μm. The results are shown in the right-hand panel of Fig. 10. Notably, there was no significant difference in the angular resolution in the lower-energy band among the different widths. This is because the uncertainty in the angular resolution is primarily attributed to multiple scattering effects within this energy range. However, as multiple scattering effects decrease at higher energy levels, the measurement uncertainty becomes more prominent, and finer silicon strips lead to better resolution. As a benchmark, we chose a silicon strip with a width of 120 μm, which provided an angular resolution of 0.05° at 50 GeV.

In this study, we investigated the effect of different CsI layers on the angular resolution. To simplify the mechanical structure and ease the manufacturing and assembly processes, the STED favors thicker CsI plates with fewer layers. However, thicker CsI plates degrade the angular resolution owing to the larger deflection angle resulting in multiple scattering effects. Therefore, the thickness of the CsI plate must be set appropriately. We tested three different configurations with 4, 8, or 16 layers of CsI plates interleaved in the STED while maintaining the same total radiation length to ensure the same efficiency of pair production. The effects of different layer settings on Compton-scattering events are shown in the left panel of Fig. 11. Different layer settings had opposite effects on the angular resolution and effective area. The angular resolution decreased with increasing number of CsI layers. Because the four layers had the thickest CsI, the measured energy was the most accurate, and the corresponding reconstruction direction was the most accurate according to the Compton scattering equation. However, the effective area increased with an increase in the number of CsI layers. The 4-layer CsI configuration exhibited

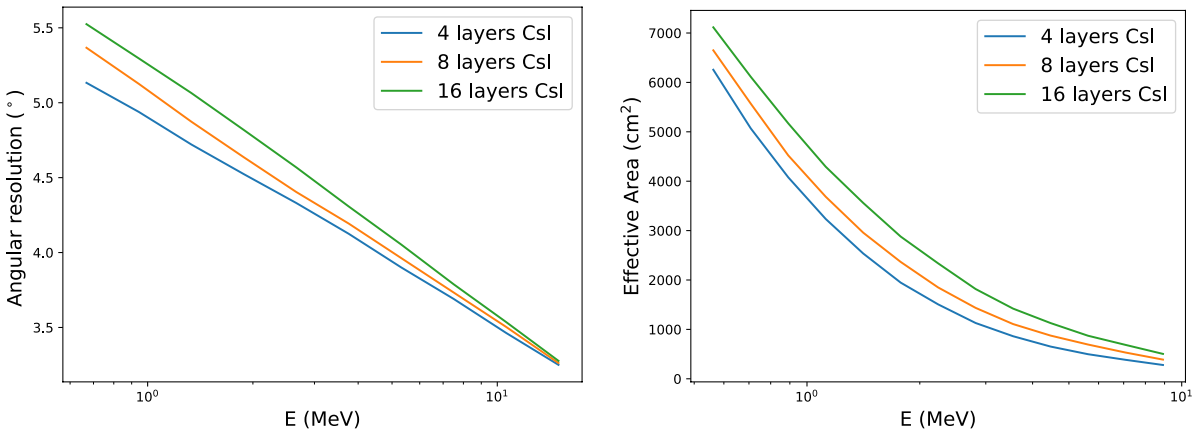

Fig. 11 (Color online) Angular resolution (left) and effective area (right) of VLAST for different configurations of CsI layers for Compton events. Normal incidence and analog readout are adopted in the simulation

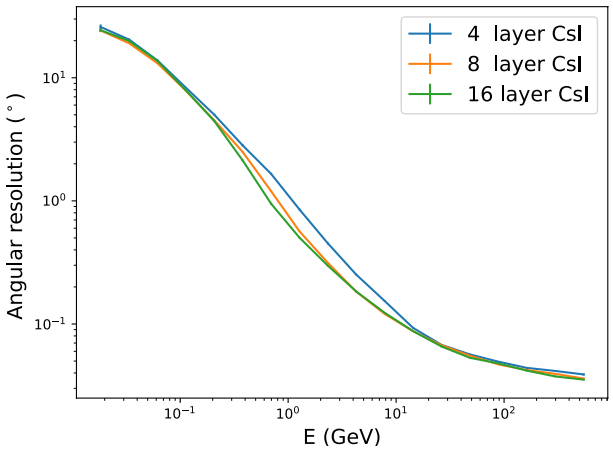

Fig. 12 (Color online) Angular resolution of VLAST for different configurations of CsI layers for pair events. Normal incidence and analog readout are adopted in the simulation

the smallest effective area. For pair production events, the effects of different CsI layer configurations on the angular resolution are shown in Fig. 12. The angular resolution was not significantly different in the low-energy band. The 16-layer configuration offers the best angular resolution at several GeV because of reduced multiple scattering in the thinner CsI. However, at several hundred GeV, the difference becomes negligible as multiple scattering effects diminish, whereas the measurement errors become more significant when the same pitch of the silicon strip is used. Different layer configurations had the same effective area because the total radiation length was the same. Based on comprehensive considerations, we determined that setting the number of CsI layers to 8 yielded the most suitable balance.

4.4 Energy resolution

Energy resolution is another critical aspect of the VLAST. One of the most interesting scientific objectives of the VLAST is the line structure in the spectra produced from astrophysical phenomena, such as de-excitation nuclear gamma-ray line emission from low-energy cosmic rays and gamma-ray lines from the annihilation of dark matter particles [70–72]. The ability to detect the line structure in the gamma ray spectrum relies significantly on the energy resolution. Here, we analyzed the energy resolution of the STED and HEIC using the above-mentioned configuration. Firstly, for pair events, the trigger conditions are MeV gamma, GeV gamma, and HEIC-HE. Second, in STED, Kalman filtering can reconstruct the photon trajectory. Third, most electromagnetic showers are contained in the HIEC. The energy deposition was obtained from the simulation, considering the statistical fluctuation error and electronic noise (based on DAMPE [73–76]) was employed for energy resolution analysis. The energy resolution was obtained after energy correction for high-energy events with more energy leakage. For Compton events, the energy was measured exclusively by the CsI calorimeter, and the uncertainty of the measurements was primarily considered in four aspects: quantum fluctuations of CsI scintillation light yield, transmission efficiency of the WLS fibers, photon detection efficiency and electronic noise of SiPMs, and the accuracy of energy calibration. The energy measurement process was simulated by randomly sampling each energy deposition of CsI using specific parameters initially estimated from previous experiments. The energy resolution was obtained using a Gaussian fit of the proportion of the sample results to the simulated real energy. The energy resolution is shown in Fig. 13. For the pair production event, a peak at approximately 100 MeV is present because the deposition body shifts from a low-energy calorimeter to the HEIC. As the number of energy particles entering the calorimeter increases, the improving energy resolution reaches 2% at a few tens of GeV. Subsequently, the resolution becomes weak owing to energy leakage. The energy resolution of the 30° and 45° incidence events was better than those of the normal-incidence events because the radiation length of the path was longer. Compared with Fermi-LAT, which has an approximate radiation length of 8.6, VLAST exhibits better energy resolution across the entire energy band owing to its deeper calorimeter, except at approximately 100 MeV.

4.5 Electron and proton discrimination

For effective photon detection, VLAST requires a strong capability to reject the charged-particle background. As previously mentioned, the proton flux is five orders of magnitude higher than that of the photons, making it difficult

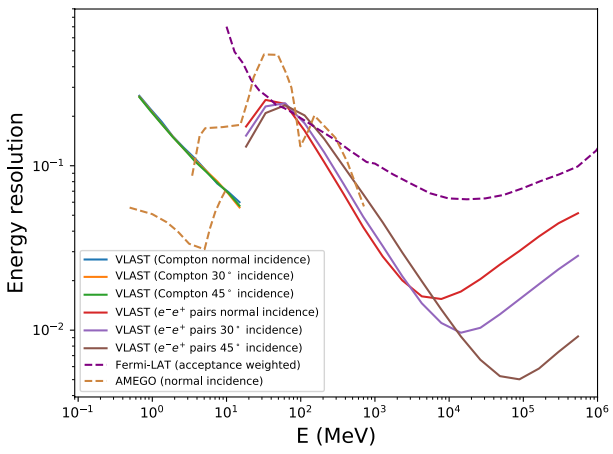

Fig. 13 (Color online) Energy resolution of VLAST for Compton and pair events with normal incidence, 30° and 45° incident angles, compare with results of AMEGO [12, 68] and Fermi-LAT [69]

to detect gamma rays in the presence of such a large background of charged particles. In addition to the ACD, the HEIC plays a crucial role in background rejection by distinguishing protons from photons based on the difference between hadronic and electromagnetic showers. To quantify the e-p discrimination ability of the VLAST, we used the ζ parameter, as in DAMPE [77], which is defined as

$$\zeta = F_{\text{last}} \times (\Sigma_i \text{RMS}_i/\text{mm})^4/(8 \times 10^6), \tag{9}$$

where F_{last} is the ratio of energy deposition in the last layer to the total energy deposition in the HEIC. The energy deposition in the last layer reflects the differences between hadronic and electromagnetic showers most significantly because BGO crystals have a large nuclear interaction length-to-radiation length ratio. RMS_i is the root-mean-square value of the energy deposited hit position in the ith layer, expressed as:

$$\text{RMS}_i = \sqrt{\frac{\Sigma_j (x_{j,i} - x_{c,i})^2 E_{j,i}}{\Sigma_j E_{j,i}}}, \tag{10}$$

where $x_{j,i}$ and $E_{j,i}$ are the positions of the hits and the deposited energy of the j-th bar in the i-th layer, respectively, and $x_{c,i}$ is the center coordinate of the shower in the i-th layer. This reflects the lateral development of the shower, which is primarily caused by the propagation of secondary particles. The secondary particles produced by hadronic showers can propagate farther than those produced by electromagnetic showers [78], which results in larger values of RMS_i.

The left panel of Fig. 14 shows the scattering distribution of $\text{RMS} = \sum_i \text{RMS}_i$ and F_{last} for protons (orange) and electrons (blue), respectively. Both the electron and proton events have energy depositions in the HEIC range of 30–100 GeV. Electrons and protons were clearly divided into two parts. The distributions of ζ parameters for the electron and proton samples are shown in the right panel of Fig. 14. A ζ value of 18 was determined to suppress proton contamination to $< 0.1\%$ while maintaining 90% electron detection efficiency. By choosing proper cuts in the ζ parameter, we can obtain the rejection fraction of the protons while maintaining 90% of the electrons, as shown in Fig. 15. At relatively low energies (several GeV), the proton rejection fraction was approximately 0.99 owing to the small size of the electromagnetic cascades. With an increase in energy, the rejection fraction increases effectively, reaching 0.999 at $\sim$ 20 GeV. Optimization of the e-p discrimination algorithm, for example, by means of machine learning, can further improve the background rejection capability [79]. Combined with the background rejection fraction of

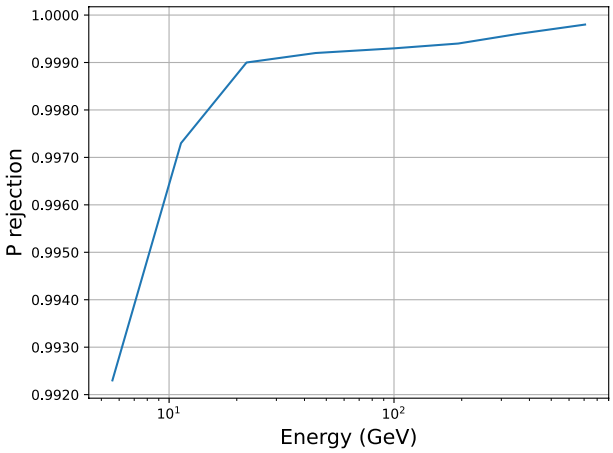

Fig. 15 The proton rejection fraction as a function of the energy deposition in HEIC when retaining 90% efficiency of electrons

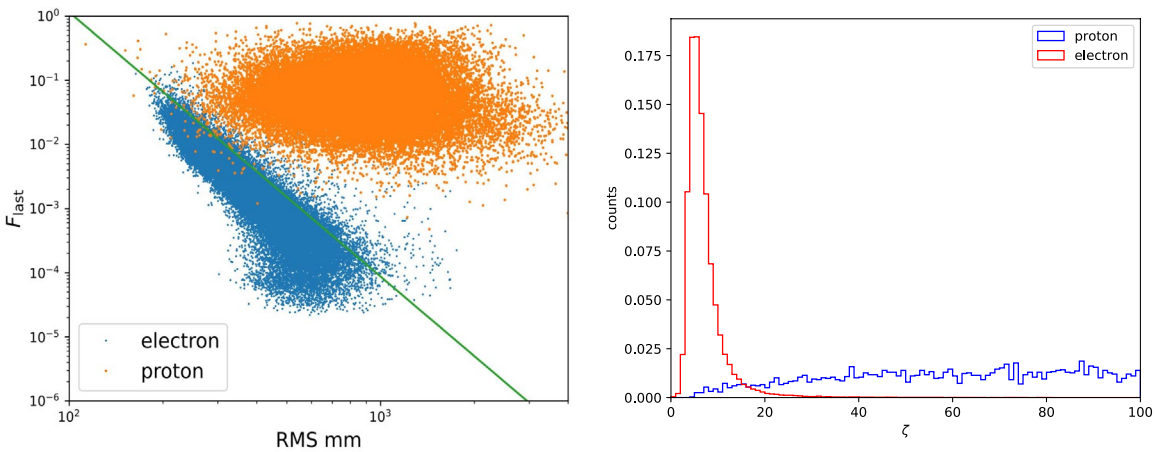

Fig. 14 (Color online) Left: Distributions of the lateral and longitudinal development of showers for electrons (blue dots) and protons (orange dots) in the HEIC. The green line illustrates the selection condition to separate these two populations. Right: One-dimensional distributions of ζ variables of electrons and protons

~ 0.999 from the ACD (design requirement) and ~ 0.9 from the STED, and based on the experience of Fermi-LAT [5], the total background rejection fraction of VLAST can reach $(1-10^{-6})-(1-10^{-7})$. Thus, VLAST has an excellent ability to detect gamma rays, even if the cosmic-ray background flux is 10^5 higher than that of the photons.

However, VLAST was not optimized for electron detection. The vertical thickness was approximately 18 radiation lengths, resulting in a relatively large leakage of electron events with energies above 1 TeV. However, given the large area of the detector, events with large incident angles can be selected to effectively increase the slant thickness of the detector. As a reference, for incident angles > 55°, the thickness is approximately 32 radiation lengths, which is comparable to that of DAMPE. If we select events with incident angles between 55° and 75°, the acceptance (for the HEIC-HE trigger) is approximately 3.5 m^2 sr. Because DAMPE can measure the electron spectrum up to approximately 15 TeV, VLAST can extend the detectable upper energy bound by at least a factor of two, even if the spectrum is as soft as E^{-4} [77]. However, the dynamic range of electronics must also be expanded to detect such high-energy events.

4.6 Detectability of gamma-ray transients

VLAST has a very good capability for exploring the γ-ray sky with an unprecedented sensitivity over a wide range of energies [21]. Considering the detection of burst-like transients as an example, we briefly discuss the potential of VLAST for such phenomena. Assuming a physical sample of gamma ray bursts (GRBs) with parameterized distributions of redshifts, luminosity, and spectra, the expected detectable quantities of GRBs can be calculated by a given detector using parameters such as the effective area, energy band coverage, PSF, and FoV [81–83]. The intrinsic parameters were obtained by comparing the simulated results with the observed sample using various detectors. The detectability can then be calculated for new detectors such as VLAST. Figure 16 shows the expected yearly rate for different fluences using VLAST and compares the expected rate by Fermi-LAT [81] and the Fermi-LAT detection rate [80] above 100 MeV. The total annual rate is approximately 43.4 for VLAST, which is approximately three times higher than that of Fermi-LAT (14.5 per year).

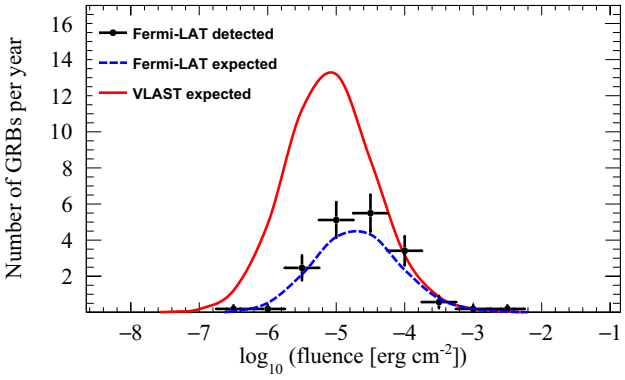

Fig. 16 (Color online) Expected detectable rate of GRBs with different fluences by VLAST (red line), compared with the detected sample [80] and the expectation [81] by Fermi-LAT

5 Summary

To validate and optimize the design of VLAST, we simulated and analyzed the performance parameters of VLAST and optimized some detailed settings such as the effective area, angular resolution, energy resolution, threshold and size of ACD, and width of the silicon strip. VLAST directly increases the gamma-ray detection capability by increasing the effective area while replacing the conventional tungsten plate used for electron pair conversion with CsI to detect Compton scattering events in the MeV band. This design allows the VLAST to have an effective area of 4 m^2, which is larger than the previous ones and smaller than the APT, but with better energy and angular resolution. The outstanding performance of VLAST can identify the uncertified point sources of Fermi-LAT, further distinguishing whether the gamma-ray excess at the center of the Milky Way originates from dark matter, whether the Fermi bubble is of leptonic or hadronic origin, and whether it fills in the gaps in the MeV band of the extragalactic background light. The design and validation of VLAST are continuing to be a subject of research. In future work, we consider incorporating additional subdetectors such as time-of-flight and neutron detectors to improve the rejection capability for complex backgrounds. Time-of-flight detectors can reduce the backsplash effect by measuring the time of recoil photons, whereas neutron detectors can improve the background rejection capability of the VLAST because hadron interactions produce large numbers of neutrons compared to electromagnetic interactions. More detailed event analysis algorithms are also under development to obtain a more accurate performance of VLAST. A prototype for validating the principles of the VLAST design is currently under development. VLAST is expected to play a crucial role in gamma-ray astronomy.

Acknowledgements The authors thank Kai-Kai Duan, Yi-Qing Guo, and Yu-Hua Yao for helpful discussions.

Author Contributions All authors contributed to the study conception and design. Material preparation, data collection and analysis were performed by Xu Pan, Wei Jiang, Chuan Yue, Shi-Jun Lei, Yu-Xin Cui, Qiang Yuan. The first draft of the manuscript was written by Xu Pan and all authors commented on previous versions of the manuscript. All authors read and approved the final manuscript.

Declarations

Conflict of interest The authors declare that they have no Conflict of interest.

References

1. W.L. Kraushaar, G.W. Clark, G.P. Garmire et al., High-energy cosmic gamma-ray observations from the OSO-3 satellite. Astrophys. J. **177**, 341 (1972). https://doi.org/10.1086/151713
2. C.E. Fichtel, R.C. Hartman, D.A. Kniffen et al., High-energy gamma-ray results from the second small astronomy satellite. Astrophys. J. **198**, 163–182 (1975). https://doi.org/10.1086/153590
3. G.F. Bignami, G. Boella, J.J. Burger et al., The COS-B experiment for gamma-ray astronomy. Space Sci. Instrum. **1**, 245–268 (1975)
4. D.J. Thompson, D.L. Bertsch, C.E. Fichtel et al., Calibration of the energetic gamma-ray experiment telescope (EGRET) for the Compton gamma-ray observatory. Astrophys. J. Suppl. Ser. **86**, 629 (1993). https://doi.org/10.1086/191793
5. W.B. Atwood, A.A. Abdo, M. Ackermann et al., The large area telescope on the fermi gamma-ray space telescope mission. Astrophys. J. **697**, 1071–1102 (2009). https://doi.org/10.1088/0004-637X/697/2/1071
6. S. Abdollahi, F. Acero, L. Baldini et al., Incremental fermi large area telescope fourth source catalog. Astrophys. J. Suppl. Ser. **260**, 53 (2022). https://doi.org/10.3847/1538-4365/ac6751
7. N.P. Topchiev, A.M. Galper, I.V. Arkhangelskaja et al., Gamma- and cosmic-ray observations with the GAMMA-400 gamma-ray telescope. Adv. Space Res. **70**, 2773–2793 (2022). https://doi.org/10.1016/j.asr.2022.01.036
8. V. Schoenfelder, H. Aarts, K. Bennett et al., Instrument description and performance of the imaging gamma-ray telescope COMPTEL aboard the compton gamma-ray observatory. Astrophys. J. Suppl. Ser. **86**, 657 (1993). https://doi.org/10.1086/191794
9. M. Kole, N. De Angelis, F. Berlato et al., The POLAR gamma-ray burst polarization catalog. Astron. Astrophys. **644**, A124 (2020). https://doi.org/10.1051/0004-6361/202037915
10. A. Zoglauer, T. Siegert, A. Lowell et al., COSI: from calibrations and observations to all-sky images. arXiv e-prints (2021). arXiv:2102.13158, https://doi.org/10.48550/arXiv.2102.13158
11. X. Wu, M. Su, A. Bravar et al., PANGU: a high resolution gamma-ray space telescope. **9144**, 91440F (2014). https://doi.org/10.1117/12.2057251
12. J. McEnery, A. van der Horst, A. Dominguez et al., All-sky medium energy gamma-ray observatory: exploring the extreme multimessenger universe. **51**, 245 (2019). https://doi.org/10.48550/arXiv.1907.07558
13. A. De Angelis, V. Tatischeff, M. Tavani et al., The e-ASTROGAM mission: exploring the extreme Universe with gamma rays in the MeV - GeV range. Exp. Astron. **44**, 25–82 (2017). https://doi.org/10.1007/s10686-017-9533-6
14. S.D. Hunter, P.F. Bloser, G.O. Depaola et al., A pair production telescope for medium-energy gamma-ray polarimetry. Astropart. Phys. **59**, 18–28 (2014). https://doi.org/10.1016/j.astropartphys.2014.04.002
15. E. Orlando, E. Bottacini, A.A. Moiseev et al., Exploring the MeV sky with a combined coded mask and Compton telescope: the galactic explorer with a coded aperture mask compton telescope (GECCO). J. Cosmol. Astropart. Phys. **2022**, 036 (2022). https://doi.org/10.1088/1475-7516/2022/07/036
16. T. Dzhatdoev, E. Podlesnyi, Massive argon space telescope (MAST): a concept of heavy time projection chamber for γ-ray astronomy in the 100 MeV-1 TeV energy range. Astropart. Phys. **112**, 1–7 (2019). https://doi.org/10.1016/j.astropartphys.2019.04.004
17. T. Aramaki, P.O.H. Adrian, G. Karagiorgi et al., Dual MeV gamma-ray and dark matter observatory - GRAMS Project. Astropart. Phys. **114**, 107–114 (2020). https://doi.org/10.1016/j.astropartphys.2019.07.002
18. C. Labanti, L. Amati, F. Frontera et al., The X/Gamma-ray imaging spectrometer (XGIS) on-board THESEUS: design, main characteristics, and concept of operation. arXiv e-prints (2021). arXiv:2102.08701
19. F. Barbato, A. Abba, A. Anastasio et al., The crystal Eye X and gamma ray detector for space missions. 37th International Cosmic Ray Conference (ICRC2021) **395**, 581 (2022). https://doi.org/10.22323/1.395.0581
20. J. Zhu, X. Zheng, H. Feng et al., MeV astrophysical spectroscopic surveyor (MASS): a compton telescope mission concept. arXiv e-prints arXiv:2312.11900 (2023). https://doi.org/10.48550/arXiv.2312.11900
21. Y.Z. Fan, J. Chang, J.H. Guo et al., Very Large area gamma-ray space telescope (VLAST). Acta Astron. Sin. **63**, 27 (2022)
22. Y. Wang, C. Feng, L. Luo et al., Study on the prototype front-end electronics for the BGO calorimeter of VLAST. **44**, 3058 (2022)
23. Q. Wan, J.H. Guo, X. Xu et al., Design of a high-dynamic-range prototype readout system for vlast calorimeter. Nucl. Sci. Tech. **34**, 149 (2023). https://doi.org/10.1007/s41365-023-01291-3
24. H.B. Yang, X.Q. Li, Y.H. Yu et al., Design and evaluation of prototype readout electronics for nuclide detector in very large area space telescope. Nucl. Sci. Tech. **33**, 65 (2022). https://doi.org/10.1007/s41365-022-01047-5
25. J. Chang, G. Ambrosi, Q. An et al., The DArk matter particle explorer mission. Astropart. Phys. **95**, 6–24 (2017). https://doi.org/10.1016/j.astropartphys.2017.08.005
26. J. Buckley, Adapt, S. Alnussirat et al., The advanced particle-astrophysics telescope (APT) project status. 655 (2022). https://doi.org/10.22323/1.395.0655
27. Z.Q. Xia, C. Zhang, Y.F. Liang et al., Searching for spectral oscillations due to photon-axionlike particle conversion using the Fermi-LAT observations of bright supernova remnants. Phy. Rev. D **97**, 063003 (2018). https://doi.org/10.1103/PhysRevD.97.063003
28. Y.F. Liang, Z.Q. Shen, X. Li et al., Search for a gamma-ray line feature from a group of nearby galaxy clusters with Fermi LAT Pass 8 data. Phy. Rev. D **93**, 103525 (2016). https://doi.org/10.1103/PhysRevD.93.103525
29. T. Bringmann, X. Huang, A. Ibarra et al., Fermi LAT search for internal bremsstrahlung signatures from dark matter annihilation. J. Cosmol. Astropart. Phys. **2012**, 054 (2012). https://doi.org/10.1088/1475-7516/2012/07/054
30. L. Wang, X.F. Han, 130 GeV gamma-ray line and enhancement of h $\rightarrow\gamma$ in the Higgs triplet model plus a scalar dark matter. Phys. Rev. D **87**, 015015 (2013). https://doi.org/10.1103/PhysRevD.87.015015
31. B. Zhou, Y.F. Liang, X. Huang et al., GeV excess in the Milky Way: the role of diffuse galactic gamma-ray emission templates. Phys. Rev. D **91**, 123010 (2015). https://doi.org/10.1103/PhysRevD.91.123010
32. M. Su, T.R. Slatyer, D.P. Finkbeiner, Giant gamma-ray bubbles from fermi-LAT: active galactic nucleus activity or bipolar galactic wind? Astrophys. J. **724**, 1044–1082 (2010). https://doi.org/10.1088/0004-637X/724/2/1044
33. B. Zhang, Extreme emission seen from γ-ray bursts. Nature **575**, 448–449 (2019). https://doi.org/10.1038/d41586-019-03503-6
34. Y. Xing, Z. Wang, Fermi study of gamma-ray millisecond pulsars: the spectral shape and pulsed emission from J0614–3329 up to 60 GeV. Astrophys. J. **831**, 143 (2016). https://doi.org/10.3847/0004-637X/831/2/143

35. Q. Yuan, B. Zhang, Millisecond pulsar interpretation of the Galactic center gamma-ray excess. J. High Energy Astrophys. **3**, 1–8 (2014). https://doi.org/10.1016/j.jheap.2014.06.001
36. Y. Xing, Z. Wang, X. Zhang et al., The likely fermi detection of the supernova remnant SN 1006. Astrophys. J. **823**, 44 (2016). https://doi.org/10.3847/0004-637X/823/1/44
37. B. Liu, Y. Chen, X. Zhang et al., GeV γ-ray emission detected by fermi-LAT probably associated with the thermal composite supernova Remnant Kesteven 41 in a molecular environment. Astrophys. J. **809**, 102 (2015). https://doi.org/10.1088/0004-637X/809/1/102
38. F. Acero, M. Ackermann, M. Ajello et al., The first fermi LAT supernova remnant catalog. Astrophys. J. Suppl. Ser. **224**, 8 (2016). https://doi.org/10.3847/0067-0049/224/1/8
39. M. Ackermann, M. Ajello, A. Allafort et al., Detection of the characteristic pion-decay signature in supernova remnants. Science **339**, 807–811 (2013). https://doi.org/10.1126/science.1231160
40. Q. Yuan, S.J. Lin, K. Fang et al., Propagation of cosmic rays in the AMS-02 era. Phys. Rev. D **95**, 083007 (2017). https://doi.org/10.1103/PhysRevD.95.083007
41. S. Chen, H.H. Zhang, G. Long, Revisiting the constraints on primordial black hole abundance with the isotropic gamma-ray background. Phys. Rev. D **105**, 063008 (2022). https://doi.org/10.1103/PhysRevD.105.063008
42. M.A. Roth, M.R. Krumholz, R.M. Crocker et al., The diffuse γ-ray background is dominated by star-forming galaxies. Nature **597**, 341–344 (2021). https://doi.org/10.1038/s41586-021-03802-x
43. S. Fermi-LAT Collaboration, M. Ackermann. Abdollahi et al., A gamma-ray determination of the Universe's star formation history. Science **362**, 1031–1034 (2018). https://doi.org/10.1126/science.aat8123
44. H. Zeng, D. Yan, Using the extragalactic gamma-ray background to constrain the hubble constant and matter density of the universe. Astrophys. J. **882**, 87 (2019). https://doi.org/10.3847/1538-4357/ab35e3
45. J.J. Wei, X.F. Wu, Testing fundamental physics with astrophysical transients. Front. Phys. **16**, 44300 (2021). https://doi.org/10.1007/s11467-021-1049-x
46. G. Amelino-Camelia, J. Ellis, N.E. Mavromatos et al., Tests of quantum gravity from observations of γ-ray bursts. Nature **393**, 763–765 (1998). https://doi.org/10.1038/31647
47. H. Li, B.Q. Ma, Lorentz invariance violation induced threshold anomaly versus very-high energy cosmic photon emission from GRB 221009A. Astropart. Phys. **148**, 102831 (2023). https://doi.org/10.1016/j.astropartphys.2023.102831
48. Z. Cao, F. Aharonian, Q. An et al., Exploring lorentz invariance violation from ultrahigh-energy γ rays observed by LHAASO. Phys. Rev. Lett. **128**, 051102 (2022). https://doi.org/10.1103/PhysRevLett.128.051102
49. J. Allison, K. Amako, J. Apostolakis et al., Recent developments in GEANT4. Nucl. Instrum. Methods Phys. Res. A **835**, 186–225 (2016). https://doi.org/10.1016/j.nima.2016.06.125
50. M. Tavani, G. Barbiellini, A. Argan et al., The AGILE mission. Astron. Astrophys. **502**, 995–1013 (2009). https://doi.org/10.1051/0004-6361/200810527
51. J. Allison, K. Amako, J. Apostolakis et al., Geant4 developments and applications. IEEE Trans. Nucl. Sci. **53**, 270–278 (2006). https://doi.org/10.1109/TNS.2006.869826
52. G. Aad, B. Abbott, J. Abdallah et al., The ATLAS simulation infrastructure. Eur. Phys. J. C **70**, 823–874 (2010). https://doi.org/10.1140/epjc/s10052-010-1429-9
53. M. He, T. Ma, J. Chang et al., GEANT4 simulation of neutron detector for DAMPE. Acta Astron. Sin. **57**, 1–8 (2016)
54. W. Jiang, Simulation of the DAMPE detector. 37th International Cosmic Ray Conference (ICRC2021) **395**, 82 (2022). https://doi.org/10.22323/1.395.0082
55. R. He, X.Y. Niu, Y. Wang et al., Advances in nuclear detection and readout techniques. Nucl. Sci. Tech. **34**, 205 (2023). https://doi.org/10.1007/s41365-023-01359-0
56. R. Qiao, W.X. Peng, G. Ambrosi et al., A charge reconstruction algorithm for DAMPE silicon microstrip detectors. Nucl. Instrum. Methods Phys. Res. A **935**, 24–29 (2019). https://doi.org/10.1016/j.nima.2019.04.036
57. Y.F. Dong, F. Zhang, R. Qiao et al., DAMPE silicon tracker onboard data compression algorithm. Chin. Phys. C **39**, 116202 (2015). https://doi.org/10.1088/1674-1137/39/11/116202
58. F. Zhang, W.X. Peng, K. Gong et al., Design of the readout electronics for the DAMPE Silicon Tracker detector. Chin. Phys. C **40**, 116101 (2016). https://doi.org/10.1088/1674-1137/40/11/116101
59. R. Qiao, W.X. Peng, D.Y. Guo et al., Charge reconstruction of the DAMPE silicon-tungsten tracker: a preliminary study with ion beams. Nucl. Instrum. Methods Phys. Res. A **886**, 48–52 (2018). https://doi.org/10.1016/j.nima.2018.01.007
60. R. Qiao, W. Peng, H. Wang et al., In 42nd COSPAR scientific assembly, the charges sharing and reconstruction study of the DAMPE silicon tungsten tracker. **42**, E1.5–91–18 (2018).
61. R. Frühwirth, Application of Kalman filtering to track and vertex fitting. Nucl. Instrum. Methods Phys. Res. A **262**, 444–450 (1987). https://doi.org/10.1016/0168-9002(87)90887-4
62. A. Cervera-Villanueva, E. do Couto e Silva, M. Ellis et al., Kalman filter tracking and vertexing in a silicon detector for neutrino physics. Nucl. Instrum. Methods Phys. Res. A **486**, 639–662 (2002). https://doi.org/10.1016/S0168-9002(01)02161-1
63. G. Evensen, The Ensemble Kalman Filter: theoretical formulation and practical implementation. Ocean Dyn. **53**, 343–367 (2003). https://doi.org/10.1007/s10236-003-0036-9
64. J.A. Hernando, The kalman filter technique applied to track fitting in glast. SCIPP **98**, 18 (1998)
65. T.S. Lu, S.J. Lei, J.J. Zang et al., Study of track reconstruction for DAMPE. Chin. Astron. Astrophys. **41**, 455–470 (2017). https://doi.org/10.1016/j.chinastron.2017.08.012
66. C. Yue, J. Zang, T. Dong et al., A parameterized energy correction method for electromagnetic showers in BGO-ECAL of DAMPE. Nucl. Instrum. Methods Phys. Res. A **856**, 11–16 (2017). https://doi.org/10.1016/j.nima.2017.03.013
67. L. Baldini, Space-based cosmic-ray and gamma-ray detectors: a review. arXiv e-prints (2014). arXiv: 1407.7631, https://doi.org/10.48550/arXiv.1407.7631
68. R. Caputo, F. Kislat, J. Racusin et al., AMEGO: simulations of the instrument performance. 35th International Cosmic Ray Conference (ICRC2017) **301**, 783 (2017). https://doi.org/10.22323/1.301.0783
69. Fermi-LAT Collaboration, Fermi LAT Performance., https://www.slac.stanford.edu/exp/glast/groups/canda/lat_Performance.htm
70. M. Ackermann, M. Ajello, A. Albert et al., Search for gamma-ray spectral lines with the fermi large area telescope and dark matter implications. Phy. Rev. D **88**, 082002 (2013). https://doi.org/10.1103/PhysRevD.88.082002
71. Y.F. Liang, Search for gamma-ray spectral lines with the DArk Matter Particle Explorer. Sci. Bull. **67**, 679–684 (2022). https://doi.org/10.1016/j.scib.2021.12.015
72. J. Chen, Y.F. Zhou, The 130 GeV gamma-ray line and Sommerfeld enhancements. J. Cosmol. Astropart. Phys. **2013**, 017 (2013). https://doi.org/10.1088/1475-7516/2013/04/017
73. Z. Zhang, Y. Zhang, J. Dong et al., Design of a high dynamic range photomultiplier base board for the BGO ECAL of DAMPE. Nucl. Instrum. Methods Phys. Res. A **780**, 21–26 (2015). https://doi.org/10.1016/j.nima.2015.01.036

74. C. Feng, D. Zhang, J. Zhang et al., Design of the readout electronics for the BGO calorimeter of DAMPE mission. IEEE Trans. Nucl. Sci. **62**, 3117–3125 (2015). https://doi.org/10.1109/TNS.2015.2479091
75. J.H. Guo, M.S. Cai, Y.M. Hu et al., Readout electronics design of prototype of BGO calorimeter in Chinese space detector for dark matter particle. Acta Astron. Sin. **53**, 72–79 (2012)
76. Y. Wei, Y. Zhang, Z. Zhang et al., Performance of the DAMPE BGO calorimeter on the ion beam test. Nucl. Instrum. Methods Phys. Res. A **922**, 177–184 (2019). https://doi.org/10.1016/j.nima.2018.12.036
77. D.A.M.P.E. Collaboration, G. Ambrosi, Q. An et al., Direct detection of a break in the teraelectronvolt cosmic-ray spectrum of electrons and positrons. Nature **552**, 63–66 (2017). https://doi.org/10.1038/nature24475
78. W. Jiang, C. Yue, M.Y. Cui et al., Comparison of proton shower developments in the BGO calorimeter of the dark matter particle explorer between GEANT4 and FLUKA Simulations. Chin. Phys. Lett. **37**, 119601 (2020). https://doi.org/10.1088/0256-307X/37/11/119601
79. Z. Xu, X. Li, M. Cui et al., An unsupervised machine learning method for electron-proton discrimination of the DAMPE experiment. Universe **8**, 570 (2022). https://doi.org/10.3390/universe8110570
80. M. Ajello, M. Arimoto, M. Axelsson et al., A decade of gamma-ray bursts observed by fermi-LAT: the second GRB catalog. Astrophys. J. **878**, 52 (2019). https://doi.org/10.3847/1538-4357/ab1d4e
81. M.M. Kang, B.Q. Qiao, Y.H. Yao et al., Prospective annual detection rate of high-energy gamma-ray bursts with LHAASO-WCDA. Astrophys. J. **900**, 67 (2020). https://doi.org/10.3847/1538-4357/aba529
82. G.G. Xin, Y.H. Yao, X.L. Qian et al., Prospects for the detection of the prompt very-high-energy emission from γ-ray bursts with the high altitude detection of astronomical radiation experiment. Astrophys. J. **923**, 112 (2021). https://doi.org/10.3847/1538-4357/ac2df7
83. Y.H. Yao, Z. Wang, S. Chen et al., Prospects for detecting γ-ray bursts at very high energies with the HADAR experiment. Astrophys. J. **958**, 87 (2023). https://doi.org/10.3847/1538-4357/ad05d1